Earth, Planets and Space

FULL PAPER

Open Access

Performance of the double-thin-shell approach for studying nighttime medium-scale traveling ionospheric disturbances using two dense GNSS observation networks in Japan

Weizheng Fu[1*], Yuichi Otsuka[1], Atsuki Shinbori[1], Michi Nishioka[2] and Septi Perwitasari[2]

Abstract

Electrodynamic coupling between the ionospheric E and F regions is widely recognized as the underlying mechanism for generating medium-scale traveling ionospheric disturbances (MSTIDs) during nighttime at midlatitudes. Recently, the double-thin-shell approach has proven to be a useful tool for studying the E–F coupling. By using total electron content (TEC) measurements, this approach enables the simultaneous reconstruction of electron density perturbations in both the E and F regions with broad and continuous coverage. However, the current reconstruction performance is limited when using only GPS-TEC measurements from GEONET, a dense network of ground-based Global Navigation Satellite System (GNSS) receivers over Japan. The expansion of available data sources and the integration of multi-GNSS observation data are considered important to enhance the double-thin-shell model. Fortunately, SoftBank Corp., a Japanese telecommunications provider, has recently developed a dense independent GNSS observation network to improve positioning services. In this paper, we analyze the potential of the improved double-thin-shell approach and emphasize the importance of incorporating multi-GNSS observation data from both GEONET and SoftBank networks. The solvability analysis, simulation, and observation results collectively indicate a substantial improvement in the spatiotemporal resolution. Specifically, the longitudinal and latitudinal resolution is improved from 0.15° to 0.1° in the E region, and from 0.5° to 0.3° in the F region. The temporal resolution is also improved from 2 to 1 min. In addition, significant improvements have been achieved in the reconstruction performance, particularly for the E region under complex background conditions. Based on these assessments, we conclude that the incorporation of GEONET and SoftBank GNSS observation data holds significant potential for improving the double-thin-shell model and advancing our understanding of MSTIDs.

Keywords GNSS TEC, Double-thin-shell model, SoftBank Corp., MSTIDs, E–F coupling

*Correspondence:
Weizheng Fu
fu.weizheng@isee.nagoya-u.ac.jp
Full list of author information is available at the end of the article

Graphical abstract

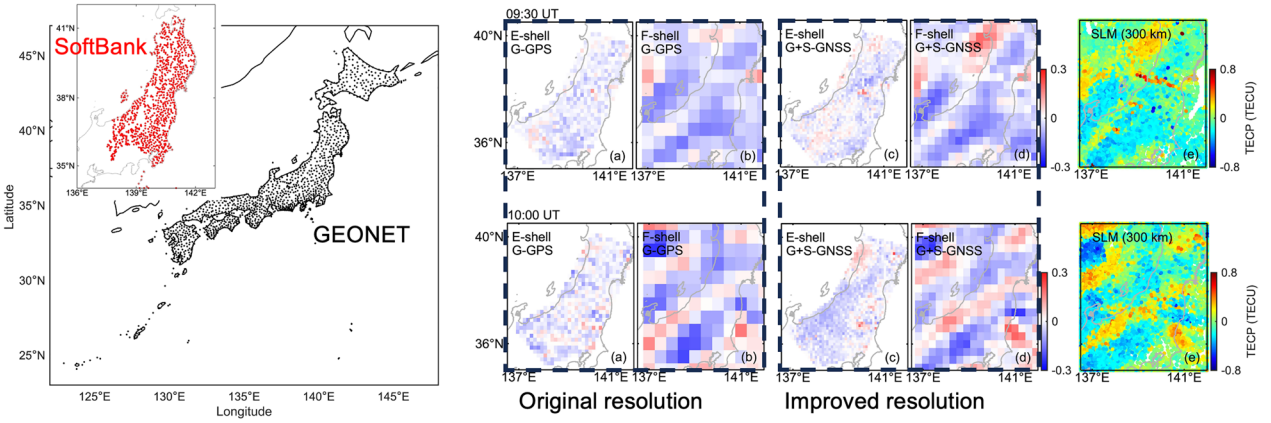

Introduction

Medium-scale traveling ionospheric disturbances (MSTIDs) are a common type of mid-latitude ionospheric disturbances that manifests as wave-like plasma density perturbations in the F region with horizontal wavelengths of a few hundred kilometers (Hunsucker 1982; Bowman 1985). Observations have shown that MSTIDs exhibit different characteristics during daytime and nighttime (e.g., Kotake et al. 2007). The generation of daytime MSTIDs can be well explained by atmospheric gravity waves (AGWs) propagating upward from the neutral atmosphere (Oliver et al. 1997), but the mechanisms underlying nighttime MSTIDs are more intricate. Previous studies have suggested that the electrodynamic force–Perkins instability in the F region plays a crucial role in the formation of nighttime MSTIDs (Perkins 1973; Kelley and Miller 1997), due to their preferred northwest–southeast (NW–SE) (or northeast–southwest (NE–SW)) alignment in the Northern (Southern) Hemisphere (Shiokawa et al. 2003; Otsuka et al. 2004). However, subsequent theoretical investigations have shown that the growth rates of typical nighttime MSTIDs cannot be explained by a Perkins instability alone (Kelley and Makela 2001; Yokoyama et al. 2008). It has been suggested that a coupled effect of polarized Es structures in the E region (known as the Es-layer instability) interacts with the Perkins instability (Tsunoda 2006; Yokoyama et al. 2009). Es (sporadic E) refers to thin layers of metallic ion plasma that typically occur in the ionospheric E region at altitudes between 95 and 125 km (Whitehead 1989). The interconnection between irregularities occurring simultaneously at different altitudes indicates the existence of a strong electrodynamic coupling process along the geomagnetic field lines during the development of nighttime MSTIDs, commonly referred to as E–F coupling (Cosgrove 2013; Otsuka 2021).

Recently, the existence of E–F coupling has been inferred by many observation results, such as ionosondes (Haldoupis et al. 2003), radars (Otsuka et al. 2007), and satellites (Liu et al. 2020). However, due to the limited observation coverage or spatiotemporal resolution of these techniques, it is difficult to identify the causal relationship during the E–F coupling process. The rapid development of the Global Navigation Satellite System (GNSS) has made it a promising tool to address this issue. In Japan, a continuous nationwide GNSS observation network operated by the Geospatial Information Authority of Japan (GSI), GNSS Earth Observation Network System (GEONET), is particularly noteworthy. This network consists of more than 1300 stations with an average spacing of about 20–25 km, which is ideal for monitoring and analyzing ionospheric disturbances in detail.

One challenge in using GNSS observations for E–F coupling is that GNSS-derived ionospheric parameters, such as total electron content (TEC), provide only two-dimensional (2-D) horizontal information on ionospheric dynamics, thus allowing perturbations caused by irregularities at different altitudes intermingle. To tackle this difficulty, Fu et al. (2022) proposed a double-thin-shell model to study E–F coupling with dense GNSS observations. This model parameterizes the perturbed ionosphere using two different shells representing the E and

F regions, and successfully provided a first continuous and broad spatial distribution of electron density perturbations in both regions. However, due to the small scale (~ 100 km in length and ~ 10 km in width) and amplitude (generally ≤ 1 TEC unit; 1 TECU = 10^{16}el/m^2) of Es layers, achieving accurate E-region reconstruction with high resolution is challenging. It not only necessitates dense ray paths, but these rays also need to be well-distributed in space to provide more information on ionospheric disturbances. At the original resolution (0.15° and 0.5° in longitude and latitude for E and F regions, respectively, 2 min in time) used by Fu et al. (2022, 2023), the E-region reconstruction performance is limited and susceptible to the F-region disturbances when relying solely on GPS observations from GEONET. In response, increasing the density of GNSS stations and incorporating multi-GNSS observation data are expected to improve the reconstruction results by providing higher resolution and fidelity. Fortunately, in late 2019, SoftBank Corp. (referred to as "SoftBank" hereafter), a Japanese telecommunications provider, constructed a dense GNSS observation network with the primary goal of providing high-precision positioning services to the public for applications such as automated driving. The SoftBank network includes more than 3300 stations, which is about 2.5 times the number of sites in the GEONET. This network has already demonstrated its capability in scientific research areas such as crustal deformation monitoring (Ohta and Ohzono 2022), and thus could potentially address the need for denser observations in ionospheric studies.

This research seeks to evaluate the applicability of the double-thin-shell model in analyzing nighttime MSTIDs by using the multi-GNSS observations from both GEONET and SoftBank networks. The primary objective is to assess the performance of the model with improved resolution. In this paper, Section "Algorithm and data" provides a concise mathematical description of the double-thin-shell approach, as well as an introduction to the data used in this analysis. Section "Solvability analysis" presents the solvability results obtained with different datasets and resolutions. Section "Simulation" demonstrates the validity and evaluates the performance of the improved model through simulation. Section "Case studies on July 3, 2022" details the reconstruction results for an MSTID event using real observations. Finally, Section "Conclusions" concludes the paper.

Algorithm and data

The typical geometric relation of double-thin-shell model is plotted in Fig. 1, wherein two pre-fixed shells are used to parameterize the three-dimensional (3-D) perturbed

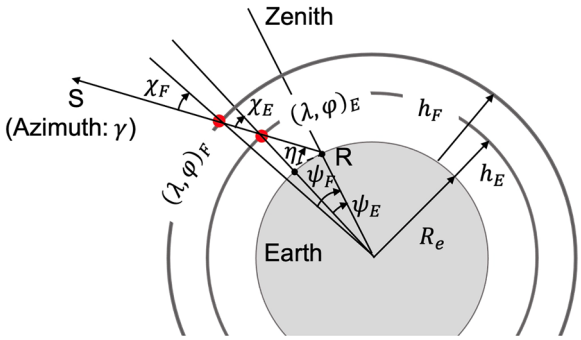

Fig. 1 Image obtained from the works of Fu et al. (2022): a typical geometric relation of the double-thin-shell model. S represents a GNSS satellite and R indicates a receiver. η and γ are the elevation and azimuth of the satellite, respectively, χ is the local satellite zenith angle, ψ is the geocentric angle, R_e represents the mean radius of the Earth, h_E and h_F represent the heights of E and F layers, respectively. Red points of intersection (λ, φ) are referred to as the ionosphere pierce points (IPPs)

ionosphere during the E–F coupling process. The hyperparameters and double-thin-shell approach used in this paper remain the same as those detailed in Fu et al. (2022), with shell heights set to 100 km and 300 km for E and F regions, respectively. The slant TEC (STEC) along the line of sight (LOS) from the receiver to the satellite was derived from dual-frequency phase and pseudorange measurements. In this paper, TEC perturbation (TECP) components are also utilized to better determine the ionospheric disturbances (Fu et al. 2022). The TECPs were obtained by subtracting a 30-min running average (centered on the LOS epoch) from each STEC value. Additionally, STEC with elevation angles smaller than 30° were excluded to mitigate multipath effects and prevent large errors in the placement of ionospheric piercing points (IPPs) when elevation angles are low; arc segments that were less than 30 min were not used to avoid any spurious perturbations. In such cases, the observed slant TECP ($TECP^S$) can be expressed as the sum of the contributions in two fixed shells:

$$TECP^S = TECP_E^S(\lambda,\varphi)_{\mathrm{E}} + TECP_F^S(\lambda,\varphi)_{\mathrm{F}}, \tag{1}$$

with $(\lambda,\varphi)_{\mathrm{E}}$ and $(\lambda,\varphi)_{\mathrm{F}}$ denoting IPPs at E- and F-region shell heights, respectively. We assumed that the ionosphere could be divided into different cells within the double-thin-shell approximation, and that the vertical TECPs within each cell in each shell were uniform. Defining χ as the local satellite zenith angle, a mixed determined system of linear equations can be constructed using M slant TECPs from GNSS observations:

$$\begin{bmatrix} \cdots & \cdots & \cdots & \cdots & \cdots \\ 0 & \sec\chi_{E_{(j-1)k}} & 0 & \sec\chi_{F_{(j-1)k}} & 0 \\ \cdots & \cdots & \cdots & \cdots & \cdots \\ 0 & \sec\chi_{E_{jk}} & 0 & \sec\chi_{F_{jk}} & 0 \\ \cdots & \cdots & \cdots & \cdots & \cdots \\ 0 & \sec\chi_{E_{j(k+1)}} & 0 & \sec\chi_{F_{j(k+1)}} & 0 \\ \cdots & \cdots & \cdots & \cdots & \cdots \end{bmatrix}_{M\times N} \begin{bmatrix} x_1 \\ \cdots \\ x_n \\ \cdots \\ x_N \end{bmatrix}_{N\times 1} = \begin{bmatrix} \cdots \\ TECP^{S_{(j-1)k}} \\ \cdots \\ TECP^{S_{jk}} \\ \cdots \\ TECP^{S_{j(k+1)}} \\ \cdots \end{bmatrix}_{M\times 1}, \quad (2)$$

where the indices j and k refer to the satellite and receiver number, respectively. The unknown vertical TEC perturbation in the nth grid is denoted by x_n, and N cells of E- and F-region unknown densities are compressed into a column vector. The total number of cells within the analyzed region, denoted as N, is determined by dividing this area into cells of specific resolutions, which is the sum of the number of cells in the E shell and the F shell. The singular value decomposition (SVD) method is used to solve this matrix equation with high fidelity, ensuring that 95% of the total variance is represented. Details can be found in Fu et al. (2022).

This study utilized all the GNSS stations from GEONET and a subset of SoftBank network (due to limited data availability). These GNSS stations receive signals from a variety of satellite navigation constellations, including GPS, GLONASS, Galileo, and BeiDou. Previously, the double-thin-shell approach relied only on GPS observations for modeling and analysis (Fu et al. 2022, 2023). In this research, we explore the possibility and evaluate the performance of incorporating multi-GNSS observation data into the approach. The spatial distribution of these GNSS stations used in this research is shown in Fig. 2a, b. The GEONET comprises over 1300 stations distributed throughout Japan, while the stations provided by SoftBank are approximately 1000, mainly concentrated in the northeast region of Honshu Island. Using only GPS observations with a 30-s data rate, each record consists of about 5000 available satellite-receiver paths for GEONET and 4000 for SoftBank network. When multi-GNSS observation data are added, these numbers increase to approximately 20,000. In Fu et al. (2022, 2023), the original resolution of the double-thin-shell model was set to 2 min in time, 0.15° and 0.5° in longitude and latitude for E and F regions, respectively. To identify the solvable regions, the counts of IPPs in each cell of the E- and F-region shell heights are plotted in Fig. 2c–h at the original resolution using the TEC observations at 09:00 UT (JST = UT + 9 h; Japan Standard Time), on day of year (DOY) 184, 2022. Following Fu et al. (2022), the minimum number of IPPs within a cell was set to 3 in order to ensure the statistical significance of the results. Consequently, in this analysis, the solvability performance within the analyzed region can be quantified by calculating the percentage of cells that are classified as solvable. This is expressed as N_1/N_0, where N_0 represents the total number of cells in the analyzed region, and N_1 is the number of cells containing three or more IPPs. The figure presents different cases of only GPS observation data from GEONET (c, d), GPS observation data from GEONET and SoftBank (e, f), and multi-GNSS observation data from GEONET and SoftBank (g, h) to indicate the variation of IPP counts after the inclusion of different datasets.

A higher density of IPPs in the region associates with an increased number of solvable cells, thereby ensuring higher solvability performance. Based on the results in subplots (c, d) of Fig. 2, as discussed in Fu et al. (2022), the region with the best solvability performance is mainly concentrated in central Japan at around (36° N, 138° E) when only GPS observation data from GEONET are used. Subplots (e, f) show a significant increase in IPP density in areas where SoftBank stations are densely located, after adding GPS observation data from the SoftBank network. This increase in density has the potential to improve the spatial and temporal resolution of the double-thin-shell model. Furthermore, subplots (g, h) demonstrate that the inclusion of multi-GNSS observation data has not only increased the density of IPPs but also their spatial distribution (more evident at 300 km, where the solvable region is expanded on the northwest side). This inference is supported by the spatial distribution of signal ray path azimuths at the same epoch shown in Fig. 3. The inclusion of multi-GNSS observations (GLONASS, Galileo, and BeiDou) improves the spatial distribution of ray paths, notably in the west-northwest (~270°–330°) direction, followed by the northeast (~45°) and south-southwest (~170°–225°). This improvement in ray path distribution may help enhance the resolution and ability of distinguishing perturbations in E and F regions.

Solvability analysis

The enhanced data density and improved spatial distribution of signal rays shown in Figs. 2 and 3 have inferred the potential for improving resolution of the double-thin-shell model, by incorporating multi-GNSS observations from both GEONET and SoftBank networks. This section will further provide a detailed analysis of the solvability with different datasets at the improved resolution. Same as Fig. 2c–h, Fig. 4 shows the IPP distribution of different datasets, but at improved longitudinal and

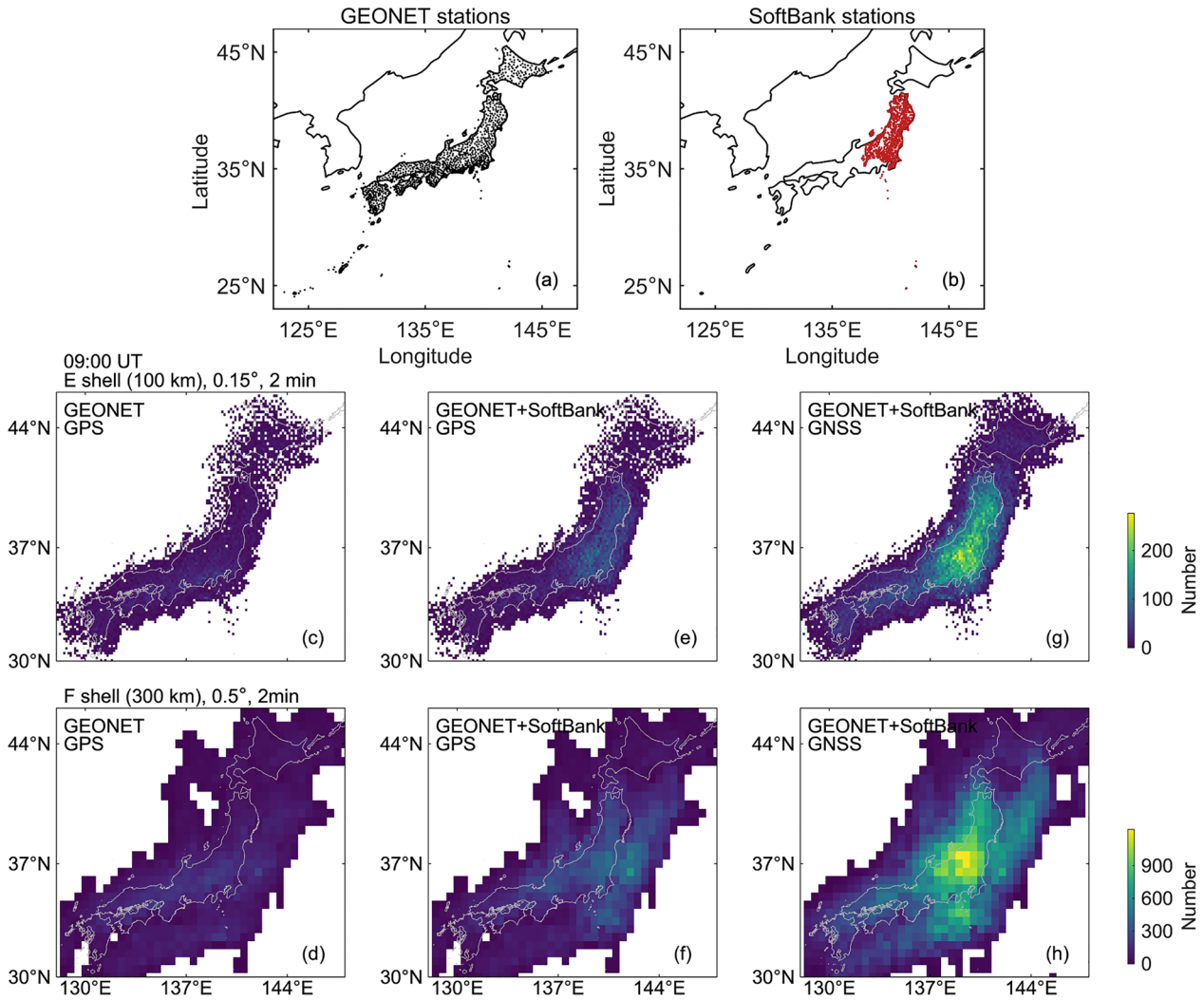

Fig. 2 **a**, **b** Distribution of GNSS stations provided by GEONET (black dots) and SoftBank Corp. (red dots). The counts of ionospheric pierce points (IPPs) in each cell of E- (middle panel) and F-region (bottom panel) shell heights, at 09:00 UT, on July 3 (day of year (DOY) 184), 2022, are displayed at the original resolution of 0.15° (**E**) and 0.3° (**F**) in longitude and latitude and 2 min in time. The IPPs are shown for the cases of using only GPS observation data from GEONET (**c**, **d**); GPS observation data from both GEONET and SoftBank Corp. (**e**, **f**); and multi-GNSS observation data from both networks (**g**, **h**)

latitudinal resolutions of 0.1° and 0.3° for E and F regions (a–f) and 0.05° and 0.15° for E and F regions (g–l). The IPP density at 100 km deserves the most focus for evaluation due to the higher resolution. Subplots (a–c) show a significant improvement in solvability after the addition of SoftBank data, even when the E-region longitudinal and latitudinal resolution is increased to 0.1°. However, from subplots (g–i), the inclusion of SoftBank data cannot increase the E-region longitudinal and latitudinal resolution to 0.05°, as there are still many grid cells with no IPPs and thus remain unsolvable. To quantify this inference, we define the analysis region by selecting the area with most data points over Japan, spanning from 33° N to 42° N and from 135° E to 143° E, as shown by the red dashed line boxes in the rightmost subplots.

We quantify the solvability by calculating the percentage of solvable grids in the analysis region. It should be noted that the solvability in the E region is expected to be lower than that in the F region, as the coverage of IPPs is much smaller at 100 km altitude. Figure 5a, b depicts the solvability of different datasets at the original resolution on DOY 184, 2022, while subplots (c–f) show the increased unsolvability resulting from the improved spatial resolution in comparison to the case at the original resolution shown in subplots (a, b). From Fig. 5c, d, at the longitudinal and latitudinal resolution of 0.1° and

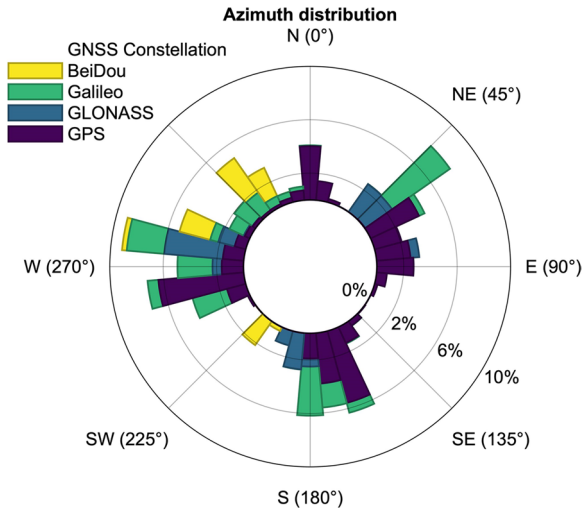

Fig. 3 Distribution of signal ray path azimuths at 09:00 UT, on July 3 (DOY 184), 2022

0.3° for E and F regions and 2 min in time, the incorporation of denser data points can effectively mitigate the impact of increased resolution. At E region, the increase in unsolvability due to improved spatial resolution is only about 4% when using GEONET (G) and SoftBank (S) multi-GNSS observations. In such a case, the solvability is even slightly better than that achieved at the original resolution with only GPS observations from GEONET. However, when the longitudinal and latitudinal resolution increases to 0.05° and 0.15° for E and F regions, the increased unsolvability reaches about 17% in the E region, even with the incorporation of multi-GNSS data from two observation networks. This would result in an incoherent reconstruction of the E region and make it difficult to distinguish perturbations of different shell heights.

The analysis above has demonstrated the feasibility of raising the spatial resolution of the double-thin-shell model to 0.1° and 0.3° in longitude and latitude for E and F regions by using GNSS observation data from GEONET and SoftBank networks. In addition, it is important to consider increasing the temporal resolution as well. At the original resolution, it was assumed that the electron density perturbations remained stationary during a 2-min interval. Now we test the case of increasing temporal resolution to 1 min. Figure 6 shows the IPP distribution and the increase in unsolvability (compared to the 2-min interval) at a temporal resolution of 1 min and a spatial resolution of 0.1° and 0.3° in longitude and latitude for the E and F regions, respectively. It can be observed that increasing the temporal resolution from 2 to 1 min has little impact on the solvability: the increased unsolvability is only about 1% for the E region and less than 1% for the F region when using multi-GNSS observation data from GEONET and SoftBank. This improvement in temporal resolution would help alleviate the issue of mixed temporal and spatial variations. As the time window decreases, the temporal and spatial mixture caused by the IPP movement within the computational epoch becomes less significant. Same as Fig. 4, the red dashed line boxes (33° N–42° N, 135° E–144° E) in Fig. 6c and f represent the region with the densest distribution of IPPs over Japan. To save computational costs and ensure accuracy, we focus on this region in the following analysis.

Simulation

Feasibility study

In this section, we conducted simulations following Fu et al. (2022) to verify the feasibility of increasing the temporal resolution to 1 min and the longitudinal and latitudinal resolution to 0.1° and 0.3° for E and F regions, respectively, when using multi-GNSS TEC observations from GEONET and SoftBank networks. The region of greatest interest for analysis is the one with the highest data density, which corresponds to the red dashed line boxes in Fig. 6c and f. The 2-D maps of simulated input disturbances are shown Fig. 7a, b. Since F-region MSTIDs typically exhibit larger amplitudes and horizontal scales than E-region structures, to enhance the clarity of the results, we set the horizontal scales of the input disturbances to about 120–180 km and 150–280 km for E and F regions, respectively; four cross structures were created in both E and F regions with amplitudes ranging from − 0.5 to 0.5 TECU at E-shell height and − 1 to 1 TECU at F-shell height. The chosen amplitudes and horizontal scales were representative of the typical wavelength and amplitude of Es and MSTIDs. IE/IF represents the ratio of the maximum input amplitude in the E region to that in the F region. The real geometry of GNSS satellites and receivers at 09:00 UT, July 3 (DOY 184), 2022, were used. With the simulated background shown in Fig. 7a, b, the integrals of perturbations along the real signal ray paths were then calculated to produce the simulated slant TECPs. No measurement noise was added in this simulation case.

Subplots (c, d) and (e, f) in Fig. 7 show the reconstruction results obtained by using GPS and multi-GNSS from GEONET (G) and SoftBank (S) networks, respectively. As the reconstruction in the F region exhibits good performance, we mainly focus on the E-region results. In subplot (c), all disturbances except **A** are successfully reconstructed, despite the relatively high background noise in the E-region reconstruction. Notably, the disturbance **A** is in the region with sparse SoftBank observations, which emphasizes the crucial role of SoftBank

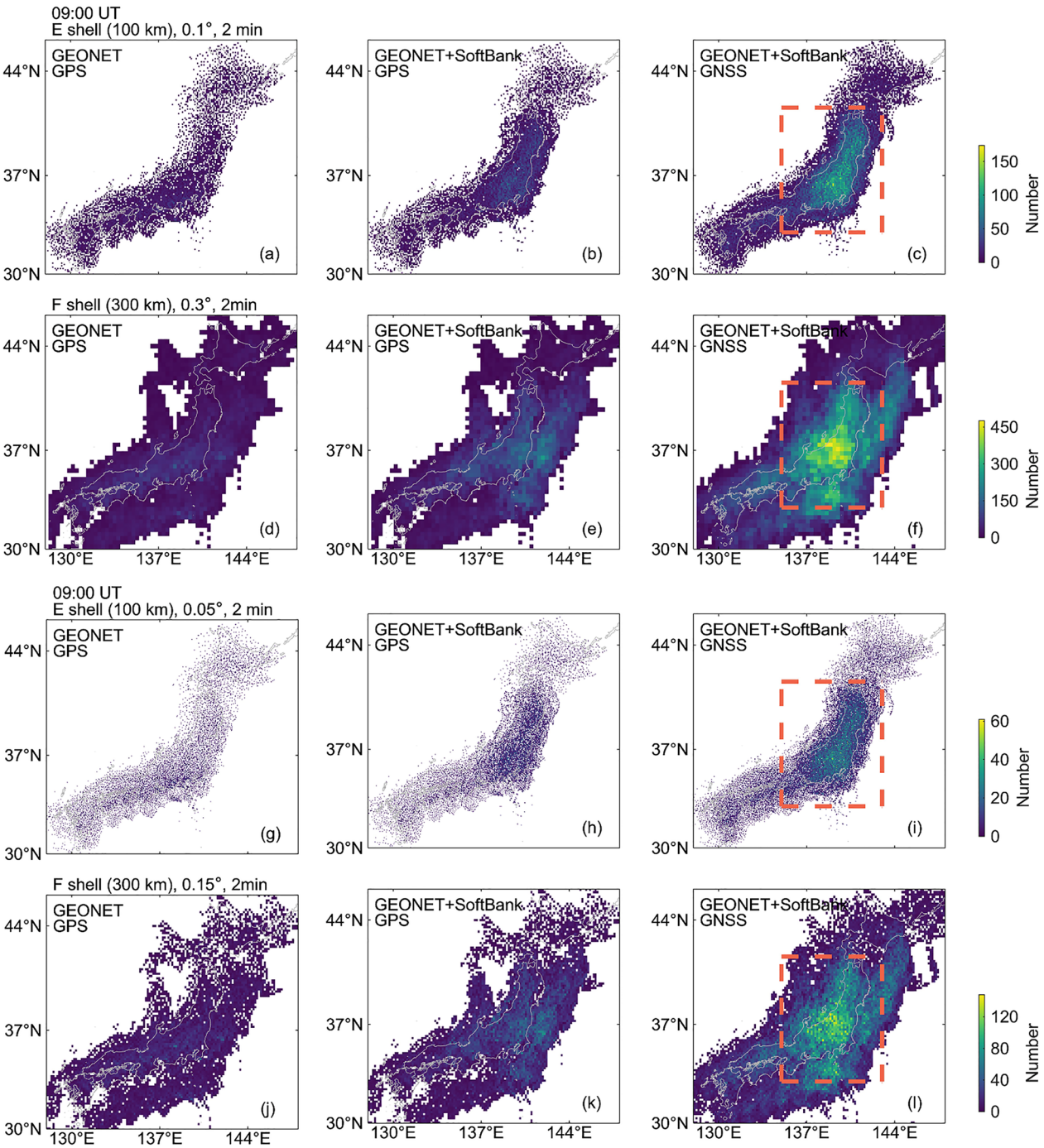

Fig. 4 Same as Fig. 2c–h but with different longitudinal and latitudinal resolution: 0.1° and 0.3° for E and F regions (**a**–**f**), and 0.05° and 0.15° for E and F regions (**g**–**l**). The red dashed line boxes in the rightmost subplots indicate the region with most data points

observation data in achieving the improved resolution. Comparing subplot (e) with (c), the reconstruction of disturbance **A** remains unsuccessful; however, there is a noticeable improvement in the background noise levels in the E-region reconstruction results. In subplot (c), the notable positive noises on the northeastern side near disturbance **B**, likely originate from the large positive simulated inputs at the corresponding location in the F region. The limited spatial distribution of signal rays in this region hinders accurate reconstruction of disturbances at

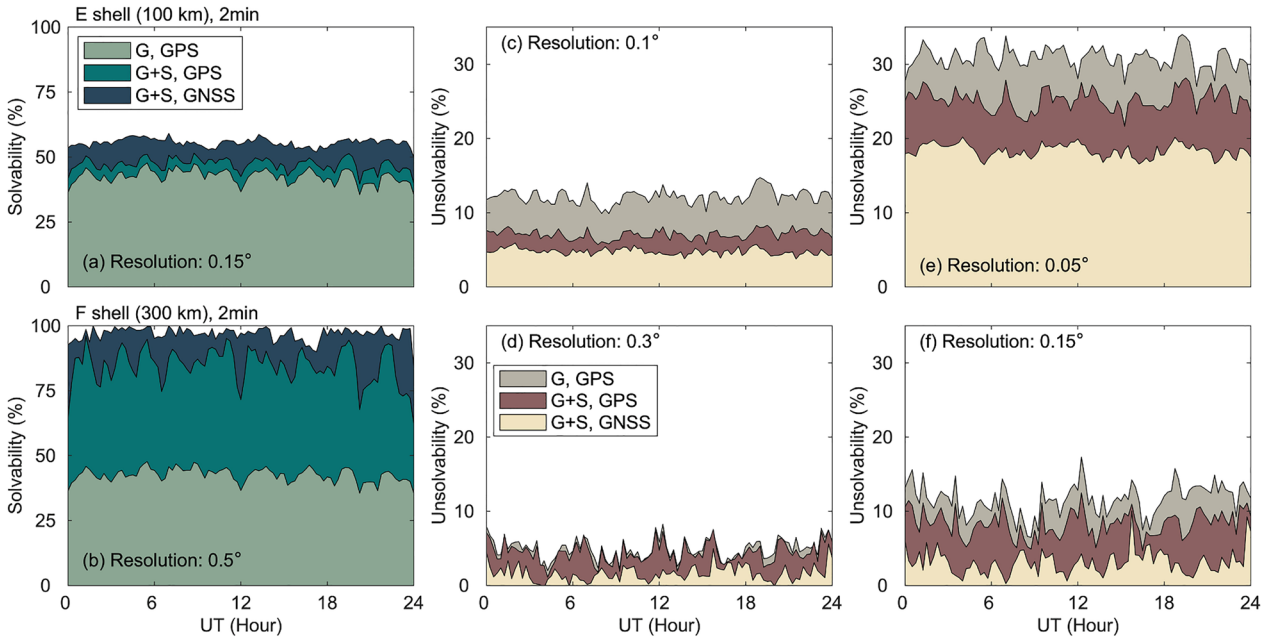

Fig. 5 **a**, **b** Solvability of different datasets at the original resolution, using GPS and multi-GNSS signal rays from GEONET (G) and SoftBank (S) on July 3 (DOY 184), 2022. **c**–**f** Increased unsolvability resulting from the improved spatial resolution when compared to the case at the original resolution shown in subplots (**a**, **b**)

the appropriate shell. The inclusion of multi-GNSS data leads to an obvious enhancement in noise reduction in this region, as evident in subplot (e). This can be attributable to the increased data density and improved spatial distribution of satellite-receiver rays, resulting in a more comprehensive sampling of the ionospheric disturbances and a more accurate representation of the electron density perturbations in the E region. Furthermore, although subplot (e) shows a reduction in background noise levels, the persistent noises observed to the left of disturbance **A** and at higher latitudes above disturbance **B** may be due to the limited spatial distribution of satellite-receiver rays at the edge of the SoftBank network. Its presence highlights the importance of considering the spatial characteristics and limitations of the GNSS network in the analysis due to the less effective sampling. To further verify the effectiveness of incorporating multi-GNSS constellations, the residual distribution using GPS and multi-GNSS signal rays from GEONET and SoftBank is shown in subplots (g) and (h), respectively. Both have small means (close to zero) and standard deviations (σ). However, despite the increase in the number of simulated observations in subplot (h), the residuals are more tightly clustered around zero, with about 95.88% of the data falling within $\mu \pm \sigma$ when using multi-GNSS observations, while in subplot (g), only about 87.37% of the data fall within this range when only using GPS observations. Based on these simulation results above, it can be tentatively concluded that enhancing the spatiotemporal resolution of the double-thin-shell model is feasible through the utilization of multi-GNSS data from GEONET and SoftBank networks.

Performance evaluation

To conduct a more comprehensive analysis of the algorithm's performance when using multi-GNSS observations from both GEONET and SoftBank, reconstructions were analyzed under various IE/IF ratios. Measurement noise is not considered in this case. The input disturbances were positioned identically as shown in Fig. 7a, b, and Fig. 8 presents 2-D maps of output disturbances at different IE/IF. The reconstruction of F region is consistently good, while the performance of E region varies. Compared to Fig. 7c, it can be seen from Fig. 8a–d that the incorporation multi-GNSS measurements still proves effective in reducing background noise at various IE/IF ratios. Although some noise persists at the edge of SoftBank network in subplots (a–c), it does not significantly impact the reconstructed disturbances in the central region. Subplots (a) and (b) show the E-region reconstruction results when input amplitude in the E region is much smaller (zero or only 1/10) than that in the F region. The maximum value of the edge background noise is about 0.16 TECU, which exceeds the maximum amplitude of the E-region input. Howerver, in subplot (c),the edge background noise level slightly increases to about 0.2 TECU and remains constant for larger input

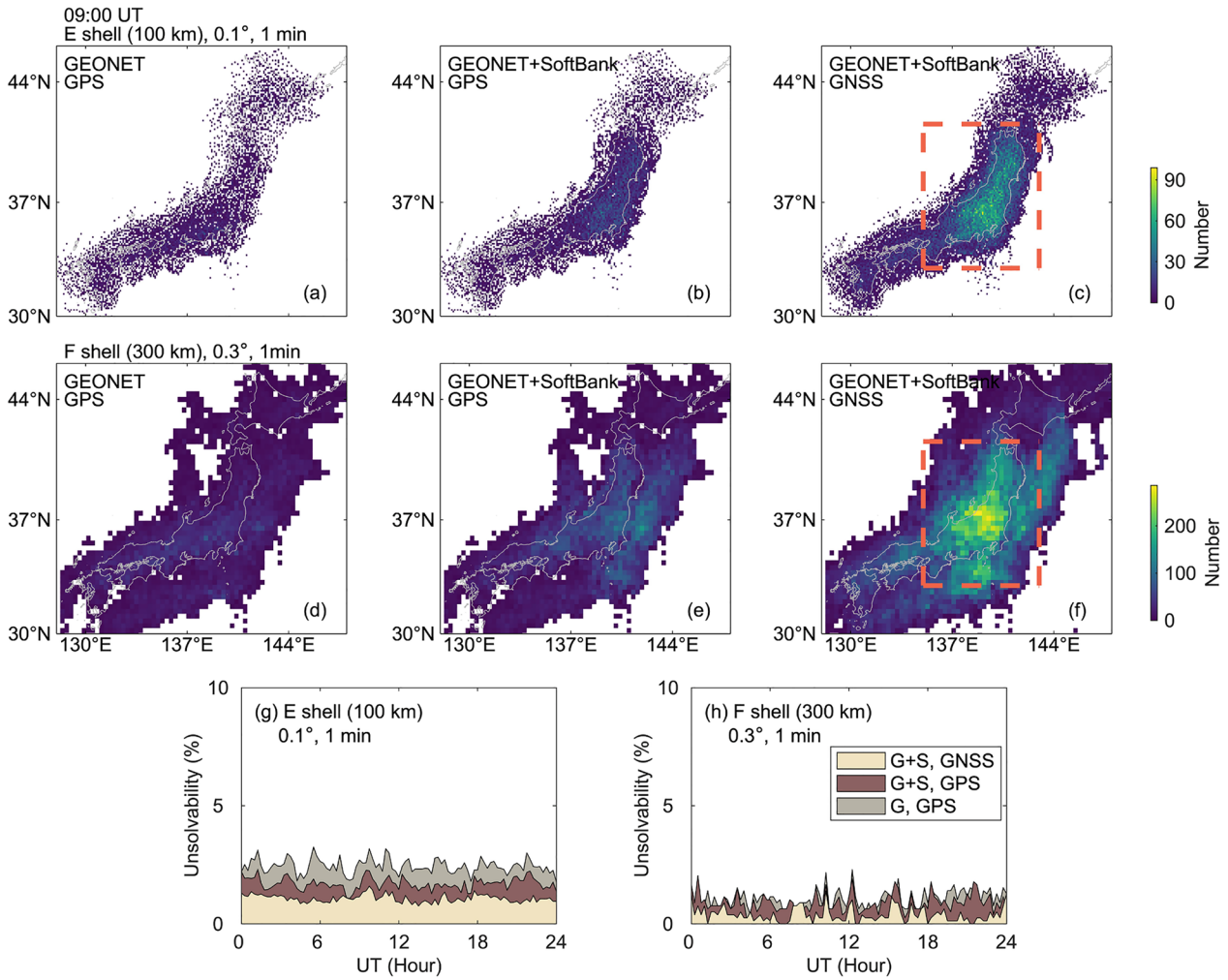

Fig. 6 **a**–**f** Same as Fig. 2c–h but with different spatiotemporal resolution: 0.1° and 0.3° in longitude and latitude for E and F regions, and 1 min in time. The area in subplots (**c**) and (**f**) marked by the red dashed line boxes represents the region with the densest distribution of IPPs over Japan. **g**–**h** Increased unsolvability resulting from the improved temporal resolution (1 min) when compared to the case at the resolution of 0.1° (**E**) and 0.3° (**F**) in longitude and latitude and 2 min in time

ampliutudes in the E region (IE/IF ≥ 0.3/1). Based on the equation $\text{foEs} = \sqrt{80.6 * \text{NmEs}}$, if we assume a 2-km thickness of Es layer (as suggested by Maeda and Heki (2014)), Es patches/layers with foEs values smaller than ~ 9 MHz may be susceptible to being affected and possibly obscured by such artificial perturbations. To mitigate the influence of background noise at E-shell height, especially at the edge of SoftBank observation network, we carefully selected a specific region characterized by higher reconstruction fidelity, as plotted by the black dashed line in subplot (a).

In contrast to subplots (a–c), the edge background noise in subplot (d) disappears when no F-region disturbance is input. That is to say, when using multi-GNSS observations from GEONET and SoftBank networks, the background noise in the E-region reconstruction could be mainly attributed to the combined effect of two factors: the large-amplitude F-region input disturbances and the limited spatial distribution of GNSS signal rays at the edge of the GNSS observation network. The region of interest selected in Fig. 8a can effectively mitigate the influence of background noise to a large extent. In fact, a similar underperformance was also observed in the simulations of Fu et al. (2022). However, in their cases, the E-region reconstruction exhibited poorer performance due to the exclusive use on GPS-TEC data. The background noise level is much higher and not limited to the boundary of the GNSS observation network. Specifically, the E-region disturbances cannot be well reconstructed even at an IE/IF ratio of 0.2/1. Therefore,

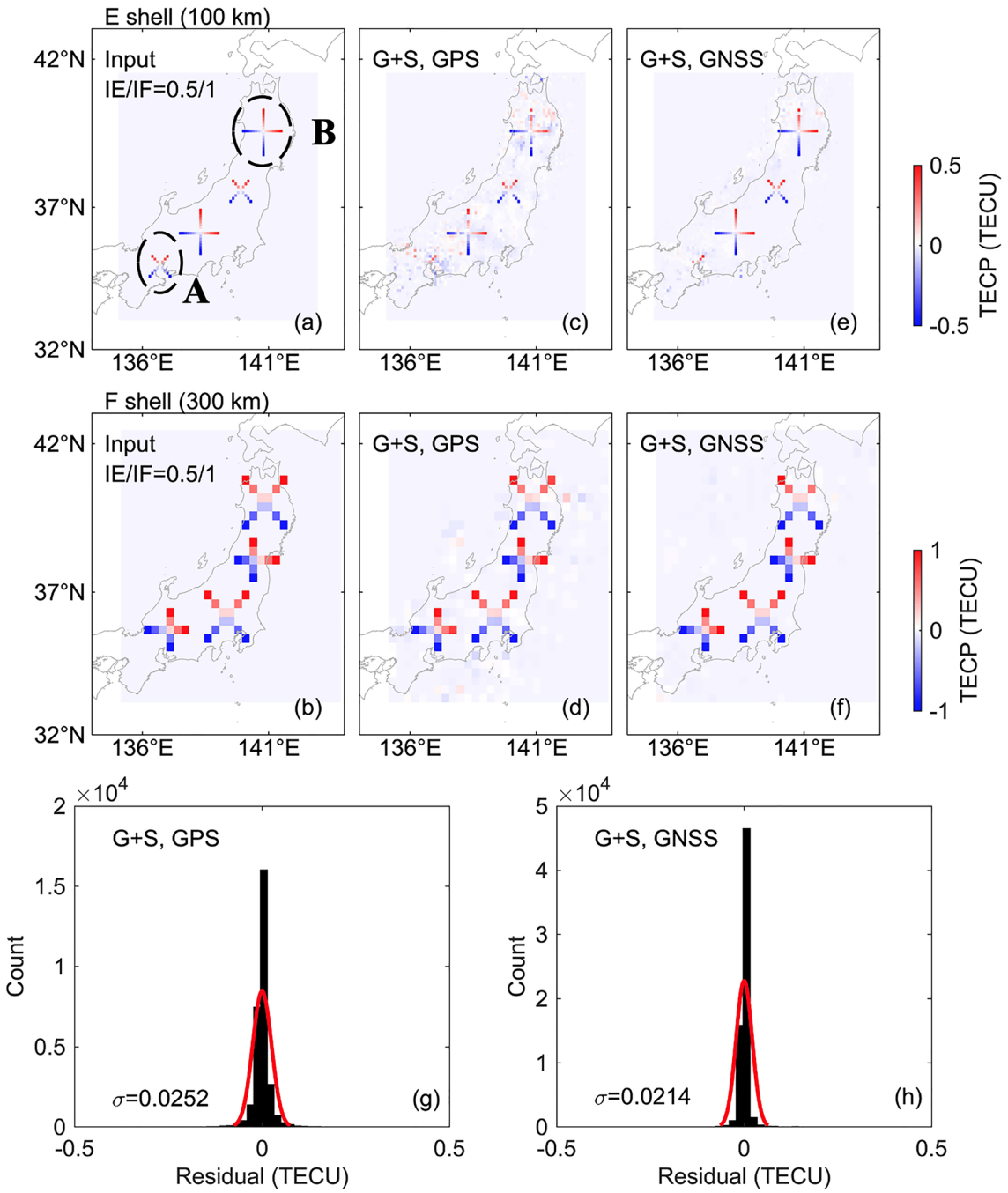

Fig. 7 2-D maps of input (**a**, **b**) and output (**c**–**f**) disturbances at E- and F-shell heights with resolution of 0.1° (E) and 0.3° (F) in longitude and latitude and 1 min in time, by using GPS and multi-GNSS signal rays from GEONET (G) and SoftBank (S) at 09:00 UT, on July 3 (DOY 184), 2022. Distribution of residuals in the corresponding cases (**g**, **h**). IE/IF represents the ratio of the maximum input amplitude in the E region to that in the F region. σ is the standard deviation of the residuals

the incorporation multi-GNSS observations from both GEONET and SoftBank networks leads to a remarkable improvement (more than doubling) in the E-region reconstruction performance, even at the improved spatiotemporal resolution.

In the following simulation, we consider the measurement noise in GNSS-TEC observations and evaluate the reconstruction performance under different noise conditions. Figure 9 presents 2-D maps of output disturbances at IE/IF = 0.5/1 under different measurement

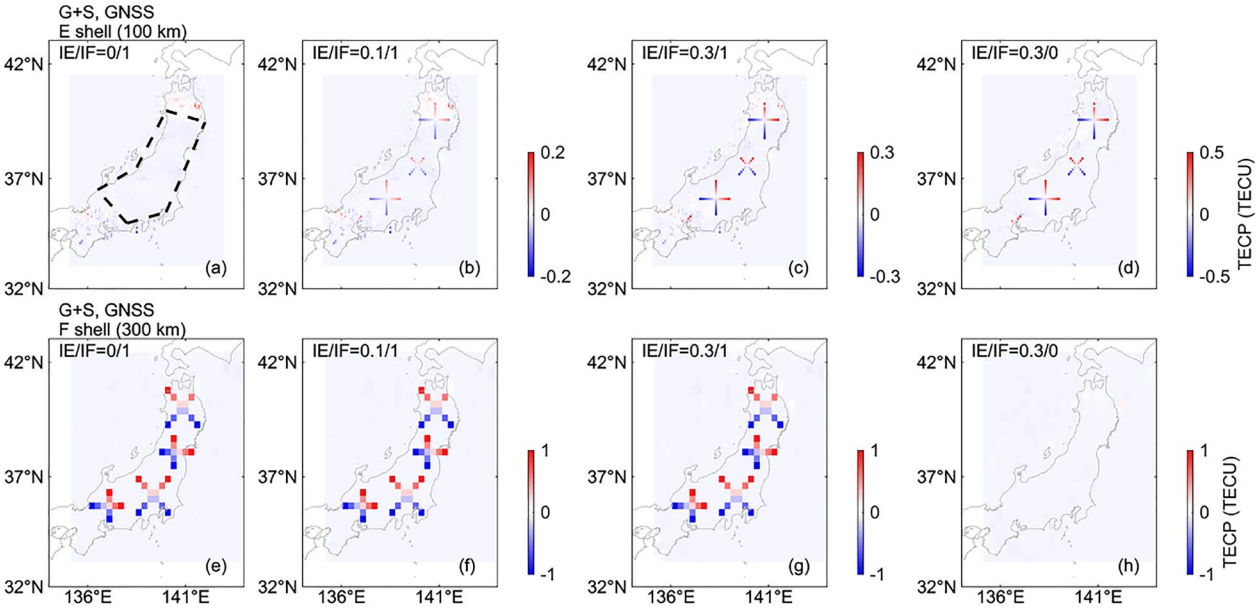

Fig. 8 2-D maps of output disturbances at different IE/IF when using multi-GNSS observations from GEONET (G) and SoftBank (S). The black dashed line in subplot (a) indicates the region with the higher reconstruction fidelity at E-shell height

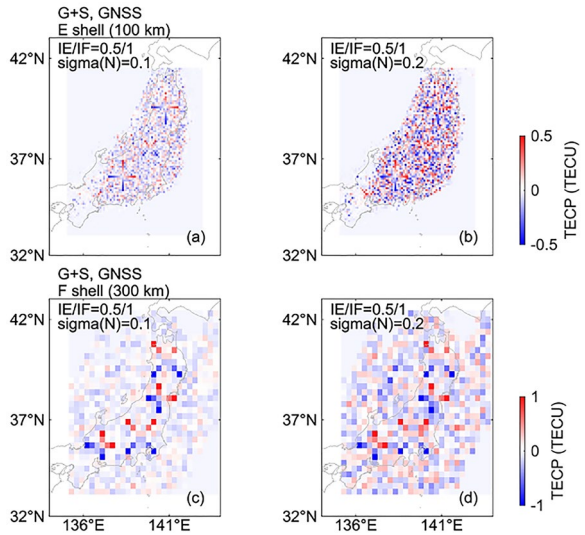

Fig. 9 2-D maps of output disturbances at IE/IF = 0.5/1 for different measurement noise levels. Sigma(N) represents the standard deviation of the Gaussian noise added to the calculation

noise levels, where sigma(N) represents the standard deviation of the Gaussian noise added to the calculation. The input disturbances were in the same position and amplitude as shown in Fig. 7a, b. From Fig. 9, the disturbances in E and F regions can still be effectively reconstructed and distinguished if the amplitude of measurement noise does not exceed the disturbance amplitude. These results are consistent with those obtained in Fu et al. (2022). The double-thin-shell approach offers theoretical advantages in reducing measurement noise compared to using absolute TEC, because instrumental biases and clock errors do not need to be considered. Additionally, by focusing on perturbations, the approach is less affected by biases arising from variations in the performance characteristics of different GNSS constellations. This allows for a more consistent and accurate estimation of ionospheric perturbations across multiple GNSS systems. It is worth noting that the choice of a 30-min window for sliding average strikes a balance between capturing Es and MSTID perturbations effectively. Using a larger window would result in poor extraction of Es perturbations, while using a smaller window would lead to the generation of spurious peaks in the MSTID data. That is to say, the measurement noise in TECPs is a crucial factor that influences the reconstruction performance of the double-thin-shell model. Efforts to improve the estimation of TEC perturbations caused by ionospheric irregularities are important for the future research.

Case studies on July 3, 2022

The simulations shown in the previous section were carried out under ideal conditions. In practical scenarios, the measurement noise may not necessarily follow a Gaussian distribution, and the disturbance structures present in the ionosphere could be more complex than what has been simulated. Therefore, we selected two different cases of the ionospheric disturbances in the E and/

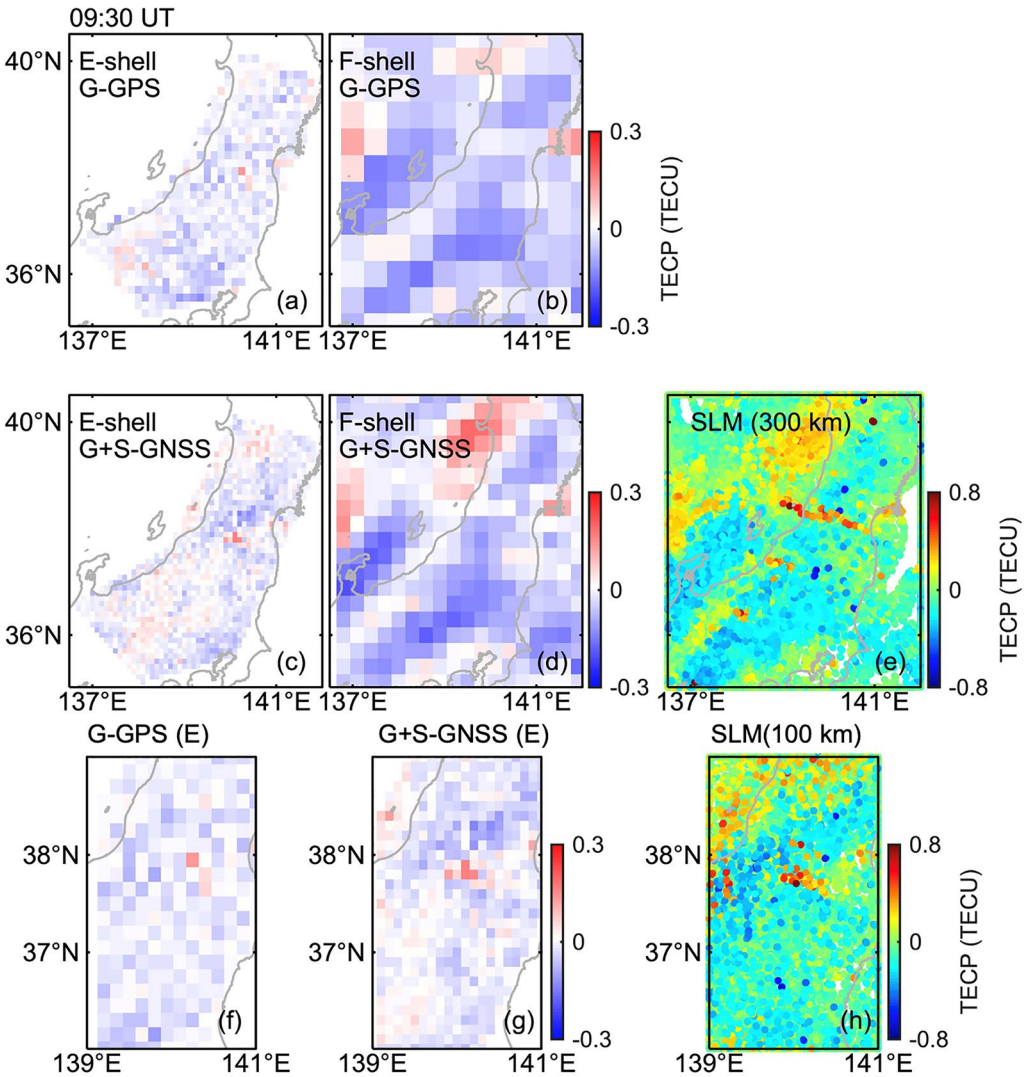

Fig. 10 The total electron content perturbation (TECP) maps at E- and F-shell heights at 09:30 UT on July 3 (DOY 184), 2022. The top (**a**, **b**) and middle two subplots (**c**, **d**) show the reconstruction results using only GPS data from GEONET and multi-GNSS data from both GEONET and SoftBank, respectively. The subplots (**e**, **h**) in the rightmost display the corresponding 2-D TECP maps obtained by using the single-layer model (SLM) at 300 and 100 km altitude, respectively. Subplots (**f**, **g**) in the bottom zoom in on the perturbed regions in subplots (**a**) and (**c**), respectively

or F regions on July 3 (DOY 184), 2022, to analyze the reconstruction performance when applying real observation data. In this day, the K index and absolute value of Dst are below 4 and 30, respectively, which typically indicate the ionosphere is in geomagnetic quiet conditions. The K index is provided by Kakioka magnetic observatory in Japan located at (36.2° N, 140.2° E).

Sporadic E during daytime

Figure 10 shows the snapshots of 2-D TECP maps at E- and F-shell heights using the double-thin-shell model at 09:30 UT before sunset in Japan. The E-shell reconstruction results are only plotted in the region with higher reconstruction fidelity as depicted in Fig. 8a. The top two subplots (a, b) show the reconstruction results using only GPS measurements from GEONET, at the original resolution of 2 min in time, 0.15° (E) and 0.5° (F) in longitude and latitude. The two subplots in the middle (c, d) are the reconstruction results obtained by using multi-GNSS measurements from both GEONET and SoftBank networks, at improved resolution of 1 min in time, 0.1° (E) and 0.3° (F) in longitude and latitude. Additionally, the rightmost subplots (e, h) present the corresponding 2-D TECP maps obtained using the single-layer model (SLM) at 300 and 100 km altitude, respectively. Subplots (f, g) in

the bottom zoom in on the perturbed regions in subplots (a) and (c), respectively.

At 09:30 UT, in subplot (e), disturbances aligned from NE to SW are observed, in addition to a distinct narrow strip perturbation at ~38° N, when using the SLM at a height of 300 km. The NE–SW aligned perturbations are caused by the daytime MSTIDs associated with AGWs. However, the E–W aligned structure with narrow width is most likely formed by daytime sporadic E at around 100 km, as the characteristics (such as positive anomalies, E–W alignment, small width) are consistent with the results observed in Maeda and Heki (2014). To be noted, the single-layer height of 300 km employed in subplot (e) cannot truly represent the horizontal structure of Es at 100-km altitude. Therefore, we plotted this TECP map at the SLM height of 100 km, as shown in subplot (h). This adjustment results in perturbations caused by Es becoming more concentrated, indicating that the width and length of the Es layer are approximately 15 km and 50 km, respectively. As expected, the double-thin-shell approach separates these two structures into the E and F regions. As obvious from the results in subplots (a–d), the NE–SW aligned perturbations are reconstructed at F-shell height, while the narrow E–W structure at ~38° N is reconstructed at E-shell height rather than F-shell height. The ability of the algorithm to accurately distinguish between E- and F-region disturbances serves as further evidence of its high fidelity and effectiveness. Furthermore, comparing subplots (f) and (g) in the bottom, subplot (g) displays a more pronounced structure of the Es layer when incorporating the multi-GNSS observations from GEONET and SoftBank networks. This suggests that the improved double-thin-shell approach has superior performance in capturing and representing the Es layer.

Nighttime MSTIDs and sporadic E

Figure 11 shows the 2-D TECP maps during 10:00–11:45 UT, which is the same as Fig. 10 but for different epochs after sunset. Subplots (p, q) and (r, s) in the bottom panel provide a closer view of the perturbations in the circled regions in subplots (a, c) and (k, m), respectively. At 10:00 UT, frontal structures aligned in NE–SW and NW–SE directions are observed to the west and east of subplot (e), respectively. The existence of NW–SE aligned frontal structures suggests the occurrence of electrodynamic forces in E and F regions (Yokoyama et al. 2009), and the disturbances with NE–SW alignment could be associated with AGWs. This inference is further supported by double-thin-shell model reconstruction results. From subplots (a–d), disturbances with NW–SE alignment are observed in both E- and F-shell heights, whereas NE–SW aligned structures are only reconstructed in the F region. This phenomenon is particularly evident when using the improved double-thin-shell approach, where the NW–SE aligned frontal structures in subplot (q) exhibit more defined patterns compared to subplot (p), and the noise level in subplot (c) is significantly reduced. These reconstruction results at this epoch demonstrate the capability of the double-thin-shell approach to accurately distinguish and separate the E region disturbances from the F region disturbances.

At 10:45 UT, nighttime MSTIDs with a noticeable NW–SE alignment become evident at ~141° E. This structure has been successfully reconstructed in the F region, as depicted in subplots (g) and (i). However, in the E-region reconstruction, the NW–SE aligned frontal structures are only captured by the improved double-thin-shell model, as shown in subplot (h). The unsuccessful reconstruction in subplot (f) could be attributed to the relatively sparse distribution of GEONET stations in this region and the small-amplitude Es layer at this time. One hour later at 11:45 UT, wave-like MSTIDs manifest over Japan. The reconstruction performance is good at F region. In the circled region of subplot (m), a distinct NW–SE aligned frontal structure is clearly reconstructed in the E region by using the improved double-thin-shell approach, which in more evident in subplot (s). In subplots (k) and (r), perturbations are also visible in this region, however, the structure is less pronounced and the location where the larger perturbations appear in subplot (s) is slightly different from subplot (r). This discrepancy might be due to the 2-min time window at the original resolution, during which the IPP movement may cause the mixture of spatiotemporal variations and the inconsistencies in location of reconstructed perturbations. In addition, the large-amplitude disturbances in the F region can weaken the reconstruction performance of the E region especially when using only GPS measurements from GEONET, as indicated by the simulation results presented in Fu et al. (2022).

Structured sporadic E: comparison with ionosonde data

Ionosondes are widely regarded as highly accurate instruments for probing and measuring the plasma density within the ionosphere. Kokubunji ionosonde (at 35.71° N, 139.49° E) is situated within the region of most GNSS-TEC data points in Japan (Fu et al. 2022), and thus can be used as a useful validation tool. It is important to note that Kokubunji is located in close proximity to the boundary of the SoftBank network. The reconstruction performance in this region is optimal when using only GEONET observation data at the original resolution. However, incorporating the SoftBank network data at the improved resolution leads to a decline in performance in

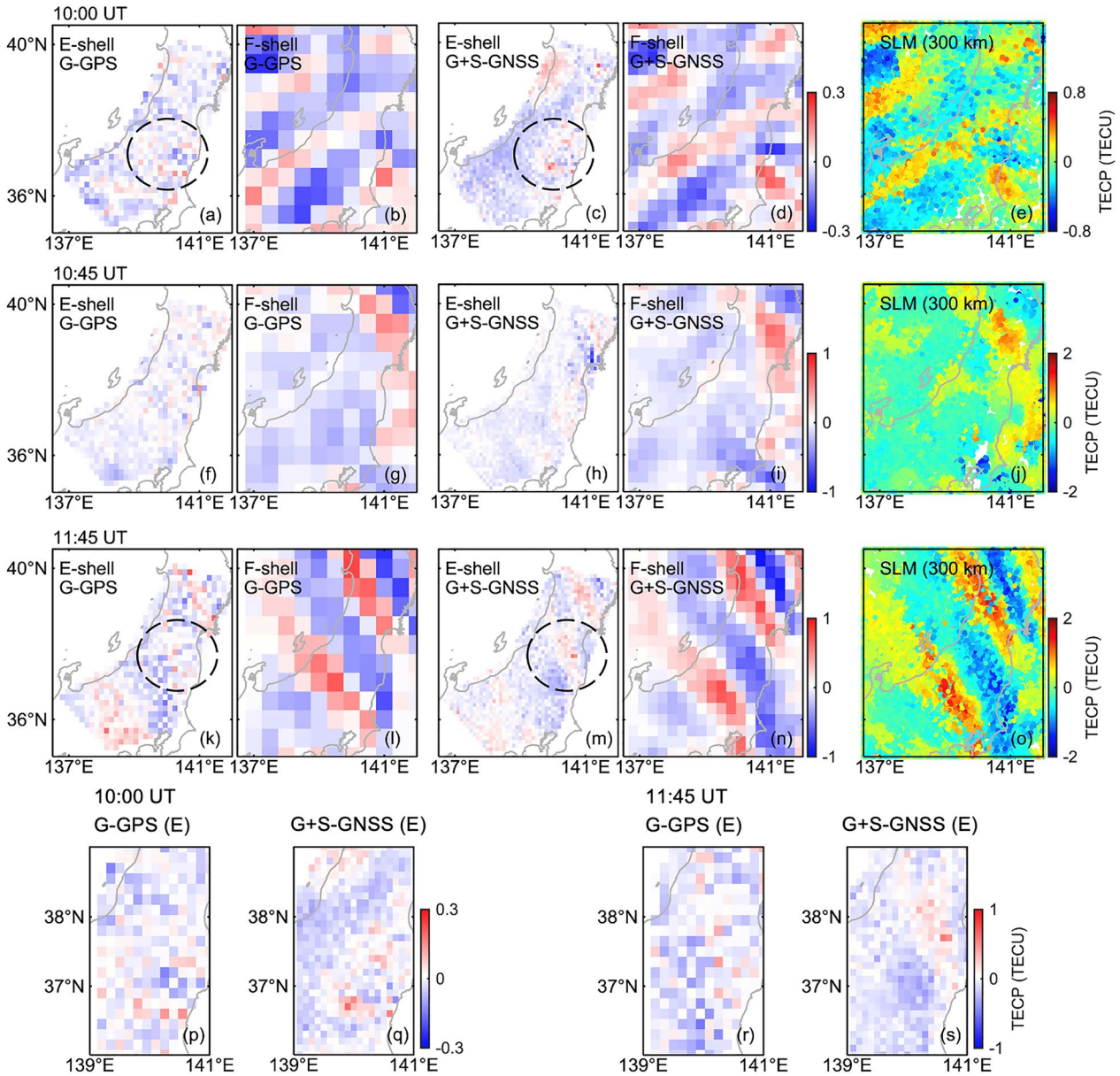

Fig. 11 Same as Fig. 10 but for different epochs after sunset. Subplots (p, q) and (r, s) in the bottom panel provide a closer view of the perturbations in the circled regions in subplots (**a**, **c**) and (**k**, **m**), respectively

this specific region due to the limited spatial distribution of signal rays, which may affect the validation results.

In the ionospheric study, foEs denotes the peak density of clumps within the Es layer, and fbEs represents minimum frequency of the F-layer trace. Radio waves within the frequency range of foEs and fbEs can be partially reflected and partially transmitted by the Es layer. The difference between foEs and fbEs (foEs – fbEs) is widely used to represent the degree of density structuring in the Es layer (Otsuka et al. 2008). For validation, we used the manual-scaled ionogram parameters (at an interval of 1 h) from Kokubunji ionosonde to evaluate the E-region reconstruction performance during this event. Figure 12 shows the time variation of the mean values of TECPs ($TECP_m$) obtained from E-region reconstruction over Kokubunji (a grid of 0.3° (0.45°) in longitude and latitude at the improved (original) resolution), as well as the Δf_{o-b} (foEs-fbEs) provided by Kokubunji ionosonde. A relatively good consistency between the variation of $TECP_m$ and Δf_{o-b} is observed, particularly during the

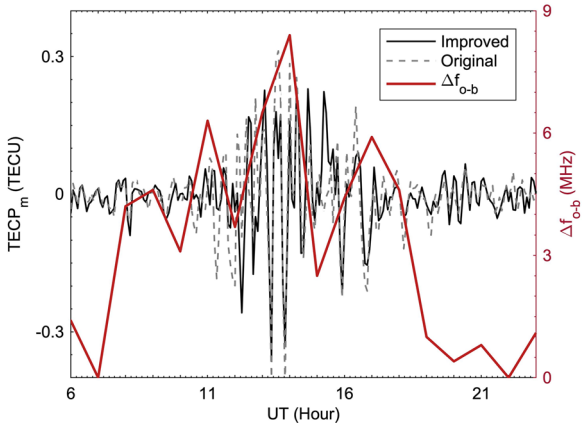

Fig. 12 The total electron content perturbation (TECP) maps at E- and F-shell heights for different epochs between 09:00 to 10:00 UT on July 3 (DOY 184), 2022

period of ~ 10:00–18:00 UT when Δf_{o-b} exhibits significant values. The underperformance observed at other time period is understandable, as it is difficult to capture the Es layer through GNSS TEC during its initial/late development phase, whose amplitudes are primarily below the GNSS noise level. The $TECP_m$ variation in the dashed line provides additional confirmation of the effectiveness of the double-thin-shell approach, even when utilizing the original resolution and solely relying on GPS measurements from GEONET. It is also worth noting that despite the proximity of the Kokubunji ionosonde to the SoftBank network boundary, $TECP_m$ obtained using the improved double-thin-shell approach (black solid line) can still reflect Es presence when Δf_{o-b} is large, albeit with a slight decrease in reconstruction amplitude.

Conclusions

The double-thin-shell approach serves as a useful tool for investigating MSTIDs. One notable advantage of this approach is the simultaneous analysis of ionospheric perturbations in E and F regions. This allows for a comprehensive understanding of the ionospheric coupled dynamics between different regions, thus providing valuable insights into the MSTIDs. However, the reconstruction performance of the double-thin-shell approach is limited when only using GPS observations from GEONET. The main objective of this study is to explore the possibilities of improving the double-thin-shell model by incorporating multi-GNSS observation data from both GEONET and SoftBank networks and assess its performance.

This research starts by conducting solvability analysis and simulations to evaluate the effectiveness of the improved model. Results confirm that integrating two dense GNSS observation networks, along with the utilization of multi-GNSS observations, leads to a substantial improvement in the spatiotemporal resolution and reconstruction fidelity. Specifically, by providing denser observations and improving the spatial distribution of signal rays, the longitudinal and latitudinal resolution improves from 0.15° to 0.1° in the E region, and from 0.5° to 0.3° in the F region. The temporal resolution has been refined from 2 to 1 min. In addition, the background noise is greatly reduced, more than doubling the E-region reconstruction performance even at improved resolution, compared to previous results that relied only on GPS observations from GEONET.

To further validate and evaluate the algorithm with the improved resolution, real observation data on July 3 (DOY 184), 2022 are analyzed to demonstrate two different cases: daytime sporadic E layer, and nighttime MSTIDs and sporadic E layer. The reconstruction results highlight the capability and fidelity of the approach to distinguish and separate E- and F-region disturbances. The effectiveness of the double-thin-shell approach is also confirmed by comparing the E-region reconstruction results with Δf_{o-b} provided by Kokubunji ionosonde. Furthermore, compared to the results using only GPS measurements from GEONET, the improved double-thin-shell approach shows a significant enhancement in reconstruction performance, particularly for the E region. Notably, the inclusion of GNSS sites from the private sector has facilitated a more detailed investigation of MSTIDs in complex background conditions, such as near the solar terminator. This suggests the feasibility of determining the role played by neutral and electrodynamic factors through a simultaneous run of the improved double-thin-shell model before and after sunset, which opens up opportunities to study the dynamics and morphology of MSTIDs comprehensively.

Abbreviations

AGW	Atmospheric gravity waves
DOY	Day of year
Es	Sporadic E
GEONET	GNSS Earth Observation Network System
GNSS	Global Navigation Satellite System
GSI	Geospatial Information Authority of Japan
IGRF	International Geomagnetic Reference Field
IPP	Ionospheric piece point
JST	Japan Standard Time
LOS	Line of sight
MSTID	Medium-scale traveling ionospheric disturbance
SLM	Single-layer model
SVD	Singular value decomposition
TEC	Total electron content
TECP	TEC perturbation
UT	Universal time
2-D	Two-dimensional
3-D	Three-dimensional

Acknowledgements
The authors thank GSI and SoftBank Corp. and ALES Corp. for providing the GNSS RINEX files.

Author contributions
FW conducted the research and prepared the manuscript. OY, SA, NM, and PS played a crucial role in the conceptualization, data processing, and paper modification. All authors read and approved the final manuscript.

Funding
This work is supported by JSPS KAKENHI (Grant Number 23K19066, 22K21345, 21H04518, and 20H00197), JSPS Bilateral Joint Research Projects no. JPJSBP120226504, and JSPS Core-to-Core Program, B. Asia-Africa Science Platforms.

Availability of data and materials
The GNSS observation data from GEONET can be accessed at Geospatial Information Authority of Japan (GSI; https://www.gsi.go.jp/ENGLISH/geonet_english.html). The SoftBank's GNSS observation data used in this study was provided by SoftBank Corp. and ALES Corp. through the framework of the "Consortium to utilize the SoftBank original reference sites for Earth and Space Science". The Dst data and K index are provided by World Data Center for Geomagnetism at http://wdc.kugi.kyoto-u.ac.jp/dstdir/index.html, and Kakioka magnetic observatory at http://www.kakioka-jma.go.jp/obsdata/obsdata.html, respectively. The ionosonde data are provided by National Institute of Information and Communications Technology (NICT) at https://wdc.nict.go.jp/IONO/.

Declarations

Ethics approval and consent to participate
Not applicable.

Consent for publication
Not applicable.

Competing interests
The authors declare that they have no competing interests.

Author details
[1]Institute for Space-Earth Environmental Research, Nagoya University, Furo-Cho, Chikusa-Ku, Nagoya 464-8601, Japan. [2]National Institute of Information and Communications Technology, 2-1 Nukuikita 4-Chome, Koganei, Tokyo 184-8795, Japan.

Received: 3 August 2023 Accepted: 22 December 2023
Published online: 08 January 2024

References

Bowman GG (1985) Some aspects of mid-latitude spread-Es, and its relationship with spread-F. Planet Space Sci 33(9):1081–1089. https://doi.org/10.1016/0032-0633(85)90027-3
Cosgrove RB (2013) Mechanisms for E-F coupling and their manifestation. J Atmos Solar Terr Phys 103:56–65. https://doi.org/10.1016/j.jastp.2013.03.011
Fu W, Yokoyama T, Ssessanga N, Yamamoto M, Liu P (2022) On using a double-thin-shell approach and TEC perturbation component to sound nighttime mid-latitude E-F coupling. Earth, Planets and Space 74(1):1–17. https://doi.org/10.1186/s40623-022-01639-w
Fu W, Yokoyama T, Ssessanga N, Ma G, Yamamoto M (2023) Nighttime midlatitude E-F coupling in geomagnetic conjugate ionospheres: a double thin shell model and a multi-source data investigation. J Geophys Res Space Phys. https://doi.org/10.1029/2022JA031074
Haldoupis C, Kelley MC, Hussey GC, Shalimov S (2003) Role of unstable sporadic-E layers in the generation of midlatitude spread F. J Geophys Res Space Physics. https://doi.org/10.1029/2003JA009956
Hunsucker RD (1982) Atmospheric gravity waves generated in the high-latitude ionosphere: a review. Rev Geophys 20(2):293–315. https://doi.org/10.1029/RG020i002p00293
Kelley MC, Makela JJ (2001) Resolution of the discrepancy between experiment and theory of midlatitude F-region structures. Geophys Res Lett 28(13):25892592. https://doi.org/10.1029/96JA03841
Kelley MC, Miller CA (1997) Electrodynamics of midlatitude spread F 3. Electrohydrodynamic waves? A new look at the role of electric fields in thermospheric wave dynamics. J Geophys Res Space Phys 102(6):11539–11547. https://doi.org/10.1029/96JA03841
Kotake N, Otsuka Y, Ogawa T, Tsugawa T, Saito A (2007) Statistical study of medium-scale traveling ionospheric disturbances observed with the GPS networks in Southern California. Earth, Planets and Space 59:95–102. https://doi.org/10.1186/BF03352681
Liu Y, Zhou C, Xu T, Wang Z, Tang Q, Deng Z, Chen G (2020) Investigation of midlatitude nighttime ionospheric E-F coupling and interhemispheric coupling by using COSMIC GPS radio occultation measurements. J Geophys Res Space Phys 125(3):e2019JA027625. https://doi.org/10.1029/2019JA027625
Maeda J, Heki K (2014) Two-dimensional observations of midlatitude sporadic E irregularities with a dense GPS array in Japan. Radio Sci 49(1):28–35. https://doi.org/10.1002/2013RS005295
Ohta Y, Ohzono M (2022) Potential for crustal deformation monitoring using a dense cell phone carrier global navigation satellite system network. Earth, Planets and Space 74(1):1–9. https://doi.org/10.1186/s40623-022-01585-7
Oliver WL, Otsuka Y, Sato M, Takami T, Fukao S (1997) A climatology of F region gravity wave propagation over the middle and upper atmosphere radar. J Geophys Res Space Phys 102(A7):14499–14512. https://doi.org/10.1029/97JA00491
Otsuka Y (2021) Medium-scale traveling ionospheric disturbances. Ionos Dyn Appl. https://doi.org/10.1002/9781119815617.ch18
Otsuka Y, Shiokawa K, Ogawa T, Wilkinson P (2004) Geomagnetic conjugate observations of medium-scale traveling ionospheric disturbances at midlatitude using all-sky airglow imagers. Geophys Res Lett 31(15):L15803. https://doi.org/10.1029/2004GL020262
Otsuka Y, Onoma F, Shiokawa K, Ogawa T, Yamamoto M, Fukao S (2007) Simultaneous observations of nighttime medium-scale traveling ionospheric disturbances and E region field-aligned irregularities at midlatitude. J Geophys Res Space Phys. https://doi.org/10.1029/2005JA011548
Otsuka Y, Tani T, Tsugawa T, Ogawa T, Saito A (2008) Statistical study of relationship between medium-scale traveling ionospheric disturbance and sporadic E layer activities in summer night over Japan. J Atmos Solar Terr Phys 70(17):21962202. https://doi.org/10.1016/j.jastp.2008.07.008
Perkins F (1973) Spread F and ionospheric currents. J Geophys Res 78(1):218–226. https://doi.org/10.1029/JA078i001p00218
Shiokawa K, Ihara C, Otsuka Y, Ogawa T (2003) Statistical study of nighttime medium-scale traveling ionospheric disturbances using midlatitude airglow images. J Geophys Res Space Phys. https://doi.org/10.1029/2002JA009491
Tsunoda RT (2006) On the coupling of layer instabilities in the nighttime midlatitude ionosphere. J Geophys Res Space Phys. https://doi.org/10.1029/2006JA011630
Whitehead J (1989) Recent work on mid-latitude and equatorial sporadic-E. J Atmos Terr Phys 51(5):401–424. https://doi.org/10.1016/0021-9169(89)90122-0
Yokoyama T, Otsuka Y, Ogawa T, Yamamoto M, Hysell DL (2008) First three-dimensional simulation of the Perkins instability in the nighttime midlatitude ionosphere. Geophys Res Lett. https://doi.org/10.1029/2007GL032496
Yokoyama T, Hysell DL, Otsuka Y, Yamamoto M (2009) Three-dimensional simulation of the coupled Perkins and Es-layer instabilities in the nighttime midlatitude ionosphere. J Geophys Res Space Phys. https://doi.org/10.1029/2008JA013789

Publisher's Note